Mechanistic Insights into Multimetal Synergistic and Electronic Effects in a Hexanuclear Iron Catalyst with a $[Fe_3(\mu_3\text{-}O)(\mu_2\text{-}OH)]_2$ Core for Enhanced Water Oxidation

Zhi-Kai Shen,[†a] Kang Li,[†b] Zi-Jian Li,[a] Yong-Jun Yuan,[c] Jie Guan,*[b] Zhigang Zou[a] and Zhen-Tao Yu*[a]

[a.] *National Laboratory of Solid State Microstructures and Jiangsu Provincial Key Laboratory for Nanotechnology, College of Engineering and Applied Sciences, Nanjing University, Nanjing, Jiangsu 210093, People's Republic of China. E-mail: yuzt@nju.edu.cn*

[b.] *School of Physics, Southeast University, Nanjing, Jiangsu 211189, People's Republic of China. E-mail: guanjie@seu.edu.cn*

[c.] *College of Materials and Environmental Engineering, Hangzhou Dianzi University Hangzhou, Zhejiang 310018, People's Republic of China.*

† These authors contributed equally to this work.

*Corresponding Author: Zhen-Tao Yu: yuzt@nju.edu.cn; Jie Guan: guanjie@seu.edu.cn;

Experimental Procedures

Materials

Tetrahydrofuran and n-butyllithium were purchased from J&K Scientific Co., Inc. Ethyl acetate, n-hexane, ammonium chloride, methanol, ethanol, ether, dichloromethane and dry acetonitrile were purchased from Taicang hushi reagent Co., Ltd. Ferrous acetate, sodium phosphate dibasic dodecahydrate, sodium phosphate tribasic dodecahydrate and sodium phosphate monobasic were obtained from Sigma-Aldrich Lab & Production Materials. $H_2{}^{18}O$ (97 atom% ^{18}O) was obtained from MERYER Co., Ltd. ^{57}Fe was purchased from ISOFLEX USA. All above solvents and reagents were commercially available and used as received without further purification. Acetone was distilled with add calcium hydride before used.

Synthesis

The H_2bipyalk ligand was prepared according to previously reported methods.[1] A mixture of ferrous acetate (240 mg) and H_2bipyalk (150 mg) in ethanol (40 mL) was stirred at 50 ^oC for 6 hours. Thereafter, the reaction mixture was cooled down, diffusion of diethyl ether into the reaction mixture gave yellow single crystals of complex **I** that were suitable for X-ray diffraction. The complex was further recrystallized 3 times for electrochemical analysis.

Characterization

Single-crystal X-ray diffraction data was obtained at 193 K on a Bruker smart Apex, with Mo Kα (λ = 0.71073 Å) radiation using ω-2θ scan mode. The data were integrated and scaled using the Bruker-SAINT software package, and all structures were solved by direct methods and refined on F^2 against full-matrix least-squares methods by using the SHELXTL V 6.12 program package.[2] Hydrogen atoms were located by geometrical calculation. All non-hydrogen atoms were refined with anisotropic thermal parameters. Crystallographic data are given in Tab. S1. Electrospray ionization-mass spectrometry (SEI-MS) analysis was performed using a Thermo scientific Q exactive mass spectrometer. ^1H NMR spectra were recorded on a Bruker AVANCE III HD 500 NMR spectrometer. X-ray photoelectron spectroscopy was performed on a Thermo Scientific K-Alpha XPS spectrometer with the binding energies corrected according to C at 284.8 eV. X-ray diffraction (XRD) studies were performed on a Bruker D8 Advance Power X-Ray Diffractometer. The ^{57}Fe Mössbauer spectra were measured by a Japanese Topologic MFD-500AV-02 Mössbauer spectrometer using the ^{57}Co(Rh) radiation source. The detector used a proportional counter, and the Doppler velocity was calibrated with a standard α-Fe foil. The Mössbauer spectra were fitted using the Lorentz absorption curve with the commercial MossWinn 3.0i software. Qualitative analysis of the phases in the samples was conducted by comparing the obtained Mössbauer parameters: the isomer shift (δ) and quadrupole splitting (Δ). Field emission scanning electron microscopy (FESEM, Zeiss, Sigma 300) were employed to

investigate the surface of electrodes before and after water oxidation. FT-IR spectra were recorded on a Nicolet iS50 FT-IR Spectrometer with KBr discs. Inductively coupled plasma optical emission spectroscopy was performed on an Agilent 5110 ICP-OES. The UV-vis absorption spectra measurements were performed in 3 mL quartz cells on a PerkinElmer LADBDA950 UV-Vis spectrophotometer. The O_2 produced was determined by using an GC9720Plus Gas Chromatograph. Dynamic light scattering (DLS) was tested by a NanoBrook 90Plus Zeta (Brookhaven, USA). All data was measured 3 times through the system. The elemental analysis experiment was completed on a Vario MICRO cube. In situ spectroelectrochemistry was performed using a honeycomb quartz cell (l = 1 mm) with a Pine 200 electrochemical workstation, where gold honeycomb was used as the working and counter electrode, and an Ag/AgCl electrode (saturated KCl in deionized water, 0.197 V vs NHE) was used as reference electrode. DEMS measurements were performed on a Hiden HPR-40 mass spectrometer in an online configuration with the electrochemical cell for gas generation analysis. Raman spectra were recorded on a Bayspec Agility 532/1064 nm Raman spectrometer (Bayspec, San Jose, CA, USA) using 532 nm laser as an excitation source. The plotted spectra are averages of 32 scans with collection times of 30 s. All spectra were intensity-corrected to the 710 and 773 cm^{-1} solvent peak of CD_3CN and CH_3CN, respectively. EQCM measurement was run on a CHI 440C EQCM workstation with an Au film-coated quartz crystal as working electrode, a Pt wire counter electrode and a Ag/AgCl reference electrode. The pH value of the solution was determined by digital pH meter (FiveEasy Plus, METTLER TOLEDO).

Electrochemical and Catalytic Water Oxidation Testing

Controlled potential electrolysis was also performed using a GC electrode (d = 3 mm) in a gas-tight cell (V = 25 mL) at a 50 mV s^{-1} scan rate. Differential pulse voltammetry (DPV) was measured with a GC electrode, ΔE = 4 mV, amplitude = 50 mV, pulse width = 4 s, sampling width = 0.167 s, pulse period = 5 s. The kinetic isotope effect (KIE) was investigated in H_2O and D_2O, respectively. The KIE value was calculated by the following eq. 1.[3] The hydrogen atom in phosphate is only 0.3 % of the total hydrogen atom in the system. ^{18}O-labeling experiments was carried out by using $H_2{}^{18}O$ for controlled potential electrolysis (0.5 mM complex **I** in a pH 7 phosphate buffer solution at 1.70 V vs NHE). At the meantime, gas products of different molecular weights generated during OER process were measured in real time by HPR-40 mass spectrometer. Oxygen production was tested in a gas-tight cell contain 0.5 mM complex **I** in a pH 7 phosphate buffer solution. The solution was deaerated by bubbling with N_2 gas for 30 min. The gas content in the headspace was determined by GC after electrolysis at 1.70 V vs NHE. The onset potential in our manuscript was derived at the intersection point of the potential-axis and the tangent at the maximum slope of the current, that is, calculated by extrapolation to zero current from the linear portion of the J–V curve.[4] The overpotential was calculated from onset by the following eq. 2.

$$KIE = \frac{k_{cat\,H_2O}}{k_{cat\,D_2O}} = \left(\frac{i_{cat\,H_2O}}{i_{cat\,D_2O}}\right)^2 \cdots\cdots(1)$$

$$\eta = V_{NHE} + 0.0591 \times pH - 1.23\,V \cdots\cdots(2)$$

Determine for Turnover Frequency (TOF)

The value of FOT can been calculated from equations below.[5,6]

$$i_{cat} = n_{cat}\,FA[cat]\sqrt{k_{cat}D} \cdots\cdots(3)$$

$$i_p = 0.4463 n_p FA[cat]\sqrt{\frac{n_p F v D}{RT}} \cdots\cdots(4)$$

$$\frac{i_{cat}}{i_p} = \frac{n_{cat}}{0.4463 n_p}\sqrt{\frac{k_{cat}RT}{n_p F v}} \cdots\cdots(5)$$

In these equations, i_{cat} is the catalytic current, i_p is the peak current, n_{cat} is the number of electrons transferred in water oxidation (4 electrons), n_p is the number of electrons transferred associated with reversible electrochemical couples (1 electron), F is Faraday's constant, k_{cat} is the pseudo-first-order rate constant, R is the universal gas constant, T is the temperature in kelvin (at a room temperature of 298K), and v is the scan rate in V/s. The TOF (k_{cat}) can be calculated from Fig. 2 in main text by eq. 6 (simplified from eq. 5).

$$k_{cat} = 0.4847 v \left(\frac{i_{cat}}{i_p}\right)^2 \cdots\cdots(6)$$

Foot of the Wave Analysis (FOWA)

Equations obtained for i/i_p versus $1/\{1+\exp[(E_0\text{-}E)F/(RT)]\}$ (WAN, eq. 7) and versus $1/\{1+\exp[(E_0\text{-}E)F/(RT)]\}^{3/2}$ (I2M, eq. 8).[7] Corresponding plots are presented in fig. S9.

$$\frac{i}{i_p} = \frac{4 \times 2.24 \left(\frac{RT}{Fv}k_{WNA}\right)^{\frac{1}{2}}}{1 + e^{\frac{F(E^0 - E)}{RT}}} \cdots\cdots(7)$$

$$\frac{i}{i_p} = \frac{4 \times 2.24 \left(\frac{RT}{3Fv}k_D C_{cat}^{\,0}\right)^{\frac{1}{2}}}{\left(1 + e^{\frac{F(E^0 - E)}{RT}}\right)^{\frac{3}{2}}} \cdots\cdots(8)$$

In these equations, F: Faradaic constant; R: gas constant; T: temperature; *i*: CV current intensity; i_p: peak current intensity of one-electron redox process of the catalyst; E_0: redox potential obtained by DPV; k_{WNA}: apparent WNA pseudo-rate constant; k_D: apparent dimerization constant. In WNA mechanisms, the TOF value can been calculated from eq. 9.

$$TOF_{max} = k_{WNA} \cdots\cdots\cdots\cdots\cdots\cdots\cdots\cdots\cdots\cdots\cdots\cdots (9)$$

Oxygen-atom Transfer Reaction

Methyl phenyl sulfide (MPS) is employed as the probe for Fe^{IV}=O based on the oxygen-atom transfer reaction.[8]

Reaction conditions: the electrolyte was H_2O/acetonitrile (1:19) mixed solution with Et_4NClO_4 (0.1 M) and MPS (1 mM), the electrolysis was conducted at 1.7 V vs NHE for 2 h, after then, the generation of methyl phenyl sulfoxide (MPSO) was determined by HPLC.

MPSO was analyzed by using Agilent high-performance liquid chromatography (HPLC), 1260 system with a C-18 column (250×3 mm, 5 µm). For the detection of MPS and MPSO, acetonitrile (65%) and water (35%) were used as the mobile phase in HPLC. The column temperature was 30 °C, the flow rate was 0.15 mL min^{-1} and the detection wavelength was 254 nm.

The number of electrons transferred was calculated[9] from:

$$N = \frac{Q}{nF} \cdots\cdots\cdots\cdots\cdots\cdots\cdots\cdots\cdots\cdots\cdots\cdots (10)$$

In this equations, N = number of moles of complex, Q = charge (coulombs), n = number of electrons, and F is the Faraday constant.

Calculation Details

The density functional theory (DFT) calculations were performed via the *Vienna ab initio* simulation package (VASP).[10] Effective potential between ionic cores and electrons was described by the projector augmented wave (PAW) method.[11] We choose the generalized gradient approximation (GGA) in the Perdew-Burke-Ernzerhof (PBE) parametrization for the exchange-correlation functional.[12] A molecule model was built, which includes 142 atoms, to study adsorption properties. The k-point sampling of the first Brillouin zone was done with a 1◊1◊1 *Γ*-centered k-points grid.[13] The energy cutoff was set to 550 eV for all cases. All the geometries were optimized using the conjugated-gradient method[14] until a Hellman-Feynman force convergence threshold of 3×10^{-2} eV/Å, with the energy differences are converged within 10^{-5} eV for each self-consistency iteration. To avoid the interactions between adjacent molecule, the vacuum region is set in excess of 20 Å. To describe the effective on-site Coulomb interactions of the transition-metal atoms in the molecule, the Hubbard-based DFT + U correction method[15] has been applied to all calculations and the effective value (U_{eff}) is set to be 3.5 eV. The reaction free energies, *ΔG*, are

determined according to the following equation:

$$\Delta G = \Delta EDFT + \Delta EZPT - T\Delta S \cdots\cdots (11)$$

where ΔE_{DFT} is the adsorption energy of a specific step, ΔE_{ZPT} is the correction of zero point energy and ΔS is the change of entropy for the reaction step. The differential charge ($\Delta\rho$) for connecting and disconnecting two parts in a structure is defined by

$$\Delta\rho(con) = \rho(part\ 1 + part\ 2) - \rho(part\ 1)\ \rho(part\ 2) \cdots\cdots (12)$$

and

$$\Delta\rho(dis) = \rho(part\ 1) + \rho(part\ 2) - \rho(part\ 1 + part\ 2) \cdots\cdots (13)$$

To obtain the ground state of the complex I, we have executed pretesting calculations inputting different initial magnetic orders and magnetic moments with consideration of different Fe oxidation states, which have enormous implications to the magnetic system during the geometric relaxation. We tested the magnetic order consisting of ferromagnetic (FM) order and anti-ferromagnetic (AFM) using the magnetic moments corresponding Fe^{2+}/Fe^{3+} high/low spin states (HS/LS). The input magnetic moments and output magnetic moments and the corresponding total energy are shown in the Tab. S5, and the counterpart of the structures are shown in Fig. S23.

The geometric optimization, excited states and *UV-Vis* spectra computations were carried out using Orca5.04 quantum-chemical packages.[16] The full geometric optimizations were performed using ORCA with using the generalized-gradient approximated Perdew–Burke–Ernzerh functional (GGA-PBE)[12,17] and Grimme dispersion correction.[18] The polarized all-electron basis sets at triple-zeta quality (def2-TZVP) and scalar relativistic versions of DKH-def2-TZVPP developed by Ahlrichs and co-workers were used for the H, C, N and O and Fe atoms.[19] The excited state computations were performed using the time-dependent density functional theory (TD-DFT).[20–22] The localized orbital bonding analysis (LOBA) for oxidation states determinations were performed using wavefunction analysis software of the Multiwfn.[23]

Results and Discussion

Tab. S1. Summary of the crystallographic and structure data for complex I.

Empirical formula	$C_{48}H_{68}N_4O_{26}Fe_6$
Formula weight	1452.16
Temperature, K	193(2)
Radiation	MoKα (*λ* = 0.71069 Å)
Crystal system	triclinic
Space group	*P*-1
A (Å)	11.422(5)
B (Å)	11.621(5)
C (Å)	12.693(5)
α (deg)	86.546(5)
β (deg)	72.856(5)
γ (deg)	68.309(5)
Volume Å^3	1493.7(11)
Z	1
Density (g / cm^3)	1.614
Absorption coefficient (mm^{-1})	1.504
F (000)	748
2 Theta range for data collection	7.132 to 49.984°
Index ranges	-11 ≤ *h* ≤ 13, -13 ≤ *k* ≤ 13 -10 ≤ *l* ≤ 15
Reflections collected	8293
Independent reflections	5098 [R_{int} = 0.0603, R_{sigma} = 0.1148]
Goodness-of-fit on F^2	1.045
Data / restraints / parameters	5098/6/383
Final R indices [I > 2 σ (I)]	R_1 = 0.0802, wR_2 = 0.1582
R indices (all data)	R_1 = 0.1646, wR_2 = 0.2268

The crystal structure of complex **I** is available free of charge from the Cambridge Crystallographic Data Centre under reference number CCDC-2300430.

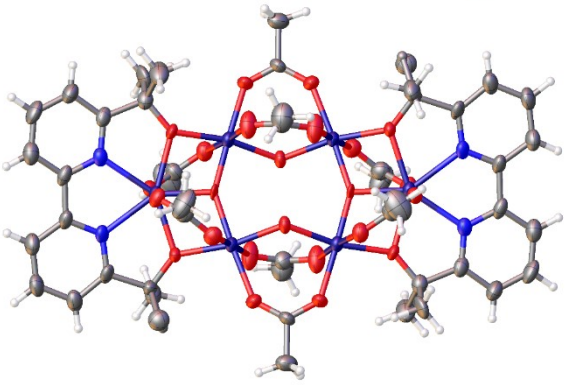

Fig. S1. X-ray crystal structure showing thermal ellipsoid plot (co-crystallized solvent molecules omitted for clarity) of complex **I**. The bridging ligands were determined to be hydroxo groups based on the analysis in main text.

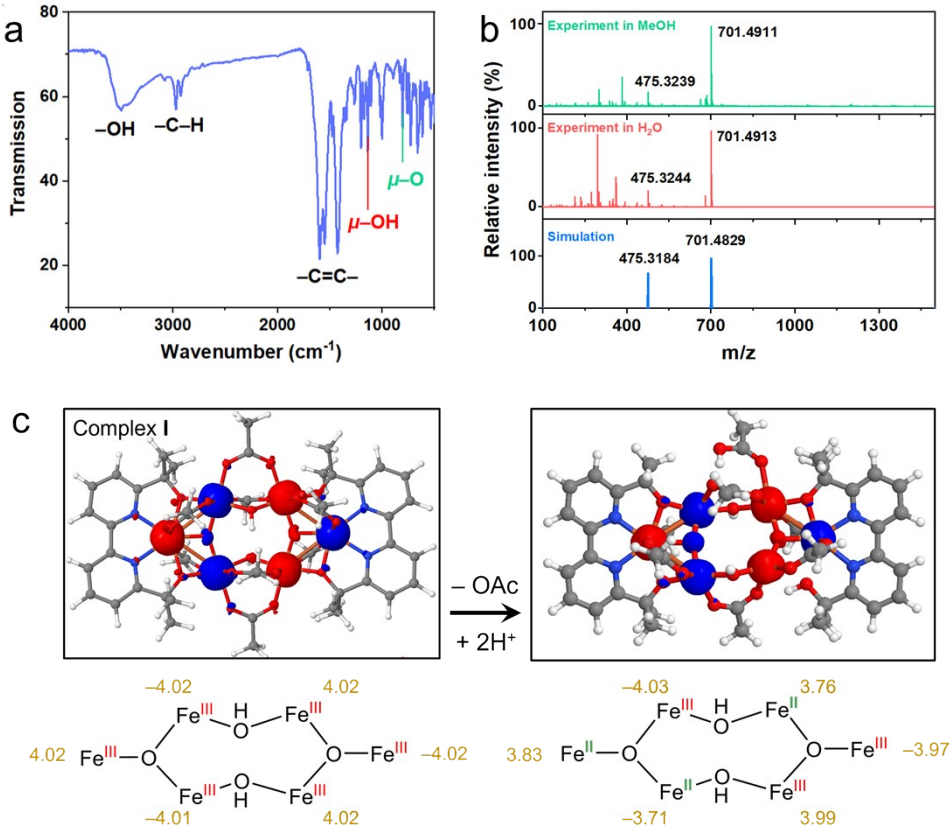

Fig. S2. a) IR spectrum (KBr) of complex **I**. The sample was dissolved in THF (extra dry), and dried completely at 70 °C under vacuum for 5 h; **b)** ESI–MS of complex **I** in MeOH and H_2O. The ion peaks at m/z ratios of 301 and 383 respectively correspond to the dibutyl phthalate and light stabilizer ions, which arise from the vial; **c)** Spin density map and Mulliken spin population analysis for complex **I** and [**I** – OAc^- + $2H^+$].

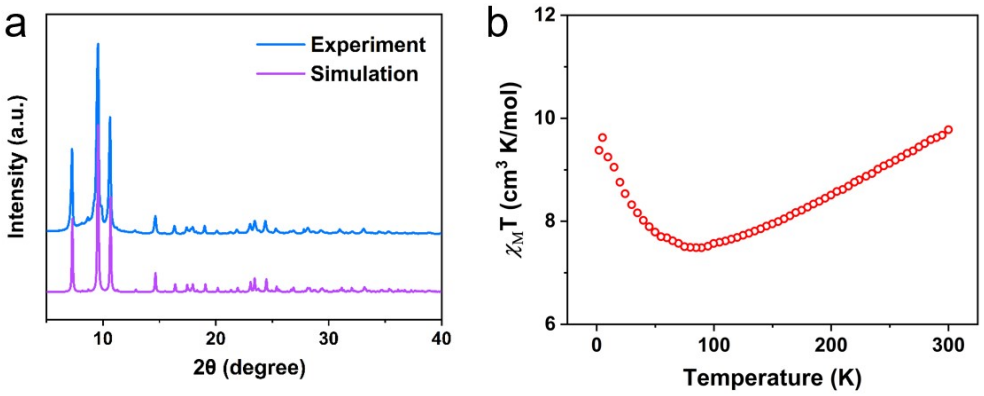

Fig. S3. a) XRD pattern of complex **I**; **b)** Temperature dependence of $\chi_M T$ at 1 k Oe in the range of 2–300 K.

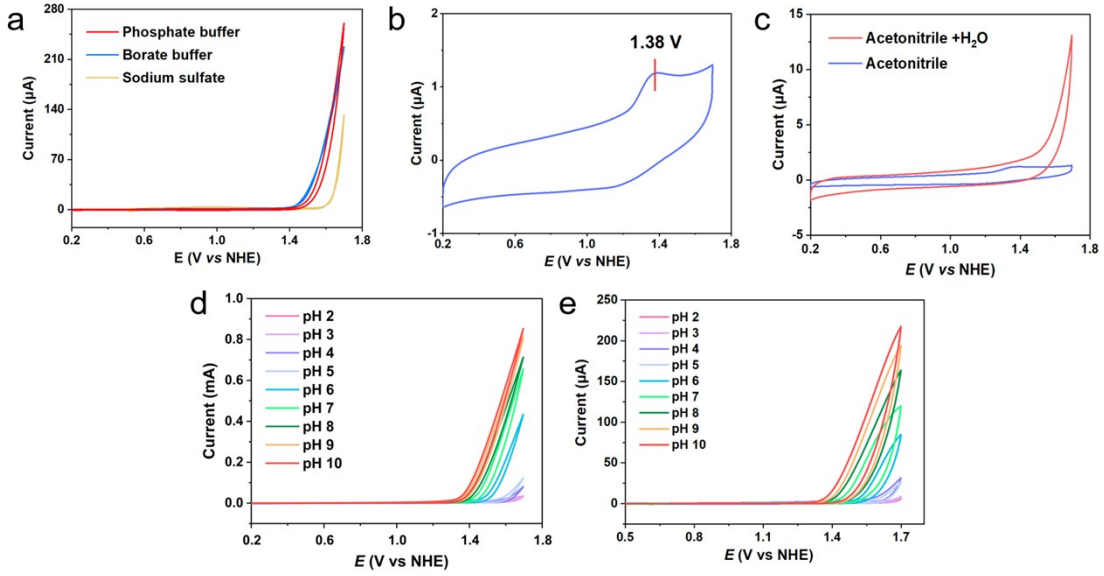

Fig. S4. a) CVs of complex **I** in different buffers with 1 cm^2 FTO electrode; **b)** CV of complex **I** (0.25 mM) in an acetonitrile solution (0.1 M Et_4NClO_4); **c)** CVs of complex **I** (0.25 mM) in an acetonitrile solution (0.1 M Et_4NClO_4) with 5% deionized water; CV curves of 0.25 mM complex **I** in different pH phosphate buffer solutions collected on **d)** a rotating ring electrode (RDE, GC, 0.2 cm^2, scan rate, 50 mV s^{-1}, rotating rate, 1600 rpm). **e)** a glassy carbon (GC, 0.07 cm^2) electrode at a scan rate of 50 mV s^{-1}.

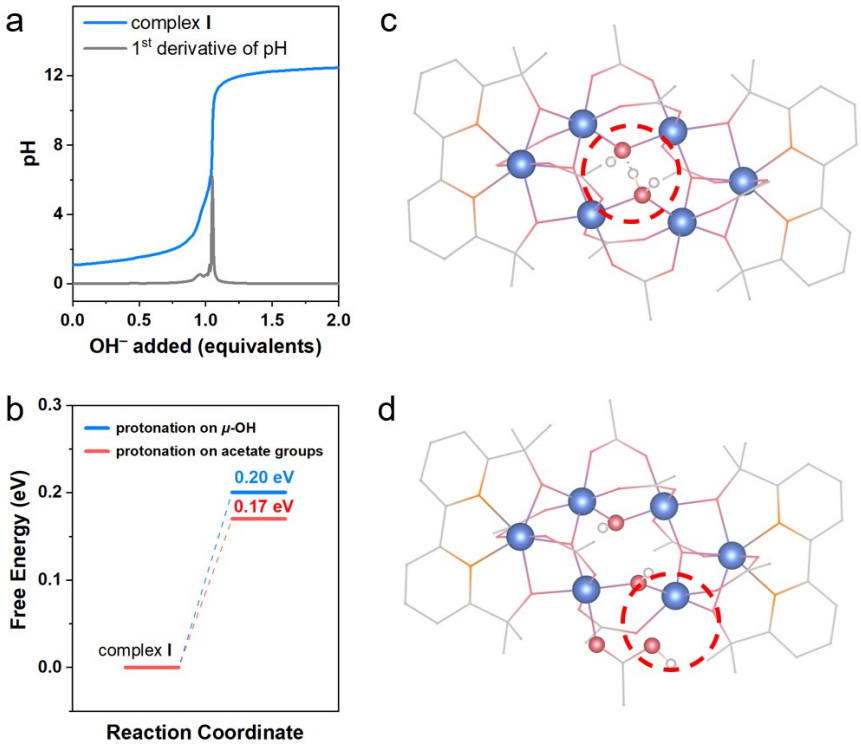

Fig. S5. a) Acid-base titration of complex **I**; **b)** The free energy barrier of protonation at μ-OH and acetate group; Structural model with **c)** μ-OH and **d)** acetate group protonated.

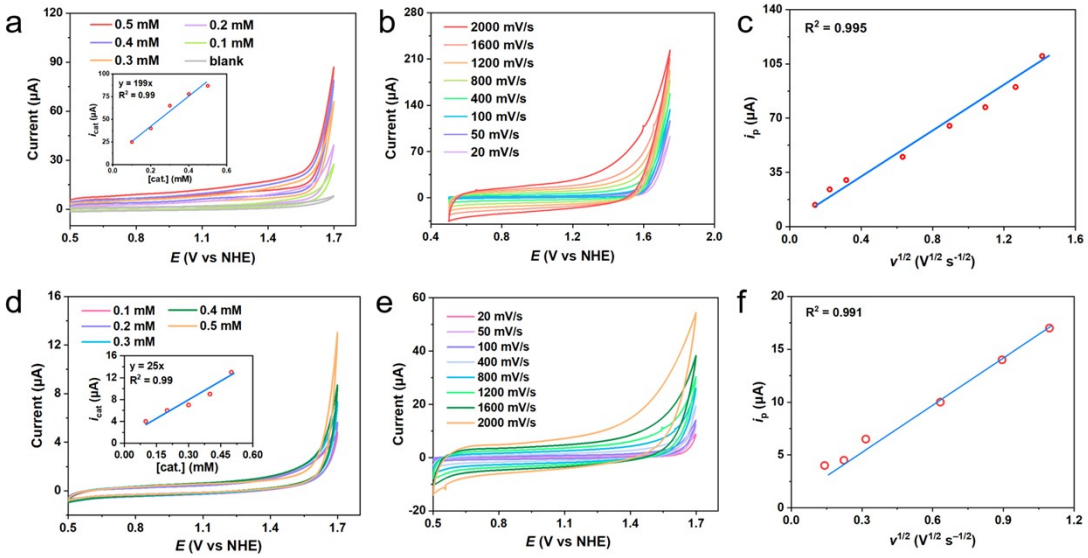

Fig. S6. Electrochemical performance of complex **I** in pH 4 phosphate buffer solution. **a, d)** CVs of complex **I** with different concentrations; Inset: plot of i_{cat} (current at 1.70 V vs NHE) against [cat.]; **b, e)** CVs of complex **I** at various scan rates; **c, f)** Plot of i_p (~1.38 V vs NHE determined from DPV) against $v^{1/2}$ from Fig. S6b. Voltammograms were collected on **(a–c)** a rotating ring electrode (RDE, GC, 0.2 cm^2, rotating rate, 1600 rpm) at a scan rate of 50 mV s^{-1} and **(d–f)** a glassy carbon (GC, 0.07 cm^2) electrode at a scan rate of 50 mV s^{-1}.

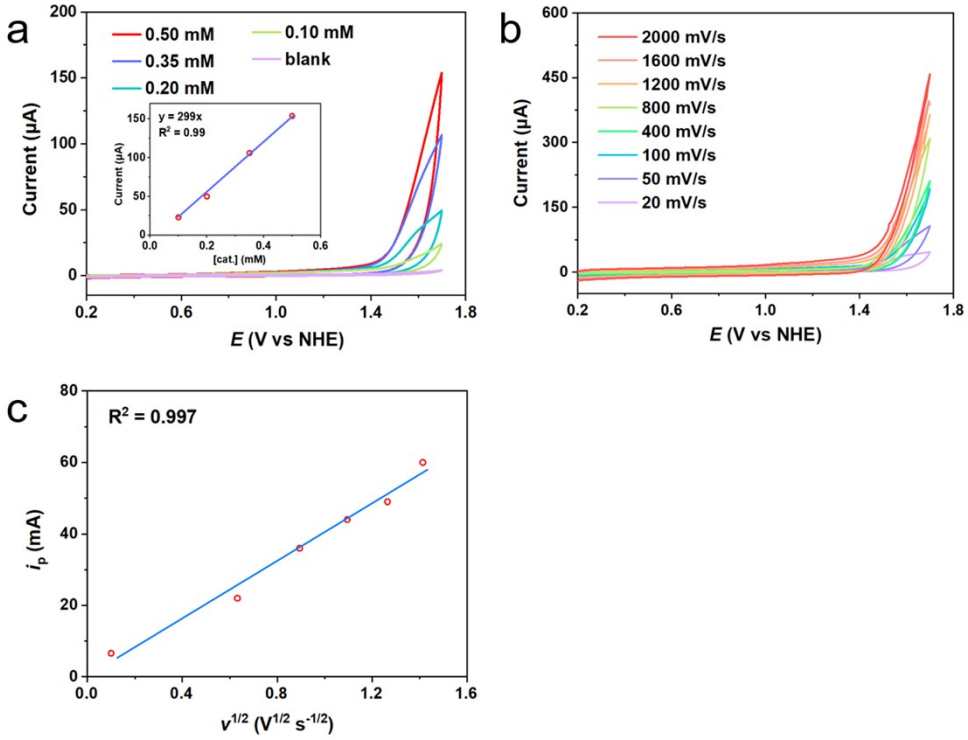

Fig. S7. Electrochemical performance of complex **I** in pH 7 phosphate buffer solution. **a)** CVs of complex **I** with different concentrations, Inset: plot of i_{cat} (current at 1.70 V vs NHE) against [cat.]; **b)** CVs of complex **I** at various scan rates i; **c)** Plot of i_p (~1.64 V vs NHE determined from DPV) against $v^{1/2}$ from Fig. S7b. Voltammograms were collected on a glassy carbon electrode (GC, 0.07 cm^2) at a scan rate of 50 mV s^{-1}.

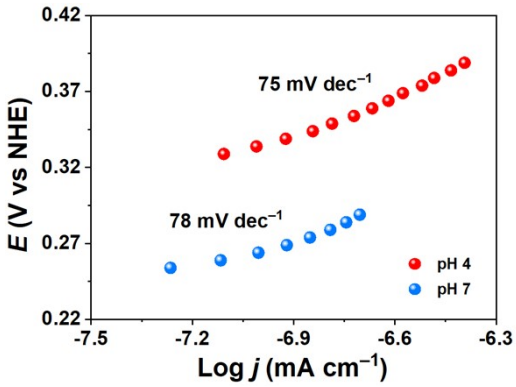

Fig. S8. Tafel slope of complex **I**.

Tab. S2. Comparison of Tafel slope among different catalysts.

Catalysts	Tafel slope	Reference
Complex **I**	75 mV dec^{-1}	this work
In–RuO_2/graphene	46 mV dec^{-1}	[24]
FTO/[Co−Fe]	70 mV dec^{-1}	[25]
$[Ir_2(pyalc)_2(H_2O)_4$-(μ-O)$]^{2+}$	174 mV dec^{-1}	[26]
IrOx	59 mV dec^{-1}	
$[Co^{III}Co^{II}(LH_2)_2(OAc)(H_2O)](DMF)(H_2O)_2$	66 mV dec^{-1}	[27]

Tab. S3. Comparison of performance in molecular catalysis for water oxidation.

Catalyst	pH	electrolyte	η (mV)	FE	TOF	Reference
complex **I**	2	phosphate buffer	290	94%	2.7 s^{-1}	This work
(Fe$\mathbf{L_1}$)$(OTf)_2$	1	aqueous CF_3SO_3H solution	370		0.1 s^{-1}	[28]
$Fe^{II}_4Fe^{III}(\mu_3\text{-}O)(\mu\text{-}\mathbf{L_2})_6]^{3+}$	2.0	CH_3CN/H_2O = 10:1	＞500	96%	1900 s^{-1}	[5]
$[Fe^{II}_4Fe^{III}(\mu_3\text{-}O)(Me\text{-}\mathbf{L_3})_6]^{3+}$	5.0	CH_3CN/H_2O = 10:1	650	92%	300 s^{-1}	[29]
$[Fe^{II}_4Fe^{III}(\mu_3\text{-}O)(Br\text{-}\mathbf{L_3})_6]^{3+}$	5.0	CH_3CN/H_2O = 10:1	710	86%	20 s^{-1}	[29]
$[Fe^{II}_4Fe^{III}(\mu_3\text{-}O)(\mathbf{L_4})_6]^{3+}$	5.0	CH_3CN/H_2O = 10:1	650	92 %	300 s^{-1}	[29]
$[Fe^{III}_6(\mu_4\text{-}O)_2(\mathbf{L_5})_2(\mathbf{L_6})_4(SCN)_4]\cdot 2MeCN\cdot 2H_2O$	7.0	0.5 M borate solution	484 [b]		[a]	[30]
$[Fe_2(\mu\text{-}O)(OH_2)_2(TPA)_2]^{4+}$	8.4	0.1M $NaHCO_3$	≈830	＞90%		[31]
$[Fe^{II}_4Fe^{III}(\mu\text{-}\mathbf{L_7})_6(\mu\text{-}O)](BF_4)_3(H_2O)_7$		CH_3CN/H_2O = 10:1			0.2–0.3 s^{-1} [1]	[32]
[(MeOH)Fe($\mathbf{L_8}$)-μ-O-($\mathbf{L_7}$)Fe(MeOH)]$(OTf)_4$		0.1M Na_2SO_4 solution	300–400		0.12 s^{-1}	[6]

$\mathbf{L}_1$ = {N,N'-dimethyl-2,11-diaza [3.3] (2,6)pyridinophane)} $(CH_3CN)_2$
$\mathbf{L}_2$ = dicarbonyl-(2,4-bis(trimethylsilyl)bicyclo[3.3.0]nona-1,4-dien-3-one)[1,3-dimethyl-ilidene]
$\mathbf{L}_3$H = bis(pyridyl)pyrazole
$\mathbf{L}_4$ = Me-bis(pyridyl)pyrazole
$\mathbf{L}_5$ = N,N,N',N'-tetrakis(2-hydroxyethyl)ethylenediamine
$\mathbf{L}_6$ = pivalic acid
$\mathbf{L}_7$H = 2,2'-(1H-pyrazole-3,5-diyl)dipyridine]
$\mathbf{L}_8$ = N,N-bis(2,2'-bipyrid-6-yl)amine

Spaces represent that the performance are not mentioned in original text.

[a] The performance was obtained based on the heterogamous catalyst formed during water oxidation.
[b] The onset potential was derived at the current density of 15 mA cm^{-2}.

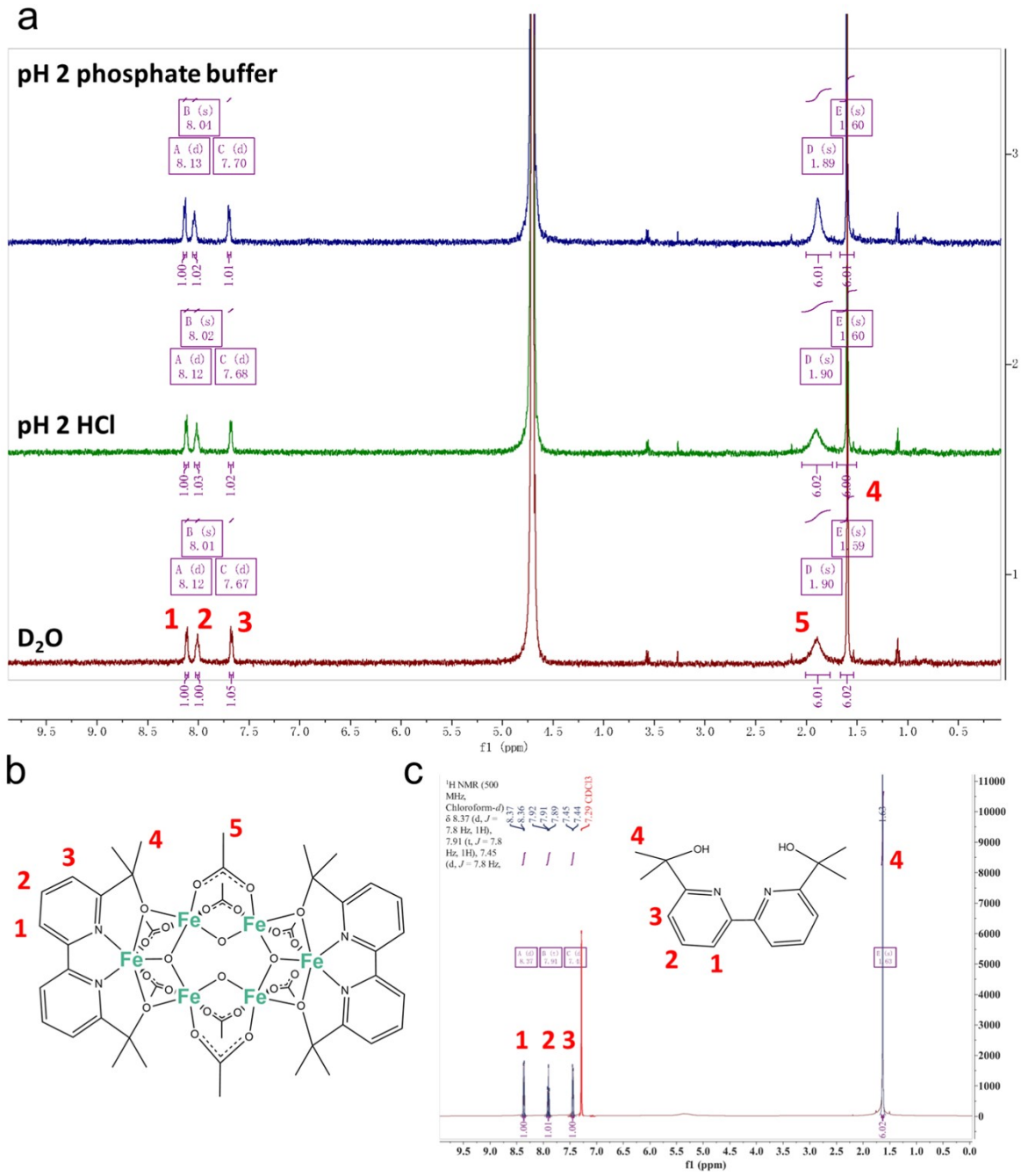

Fig. S9. a) ^{1}H NMR of complex **I** in D_2O, pH 2 D_2O adjusted by dilute HCl, and pH 2 phosphate buffer in D_2O; **b)** Schematic representation of the molecular structure of complex **I**; **c)** ^{1}H NMR of the ligand bipyalkH_2 in acetone-d_6.

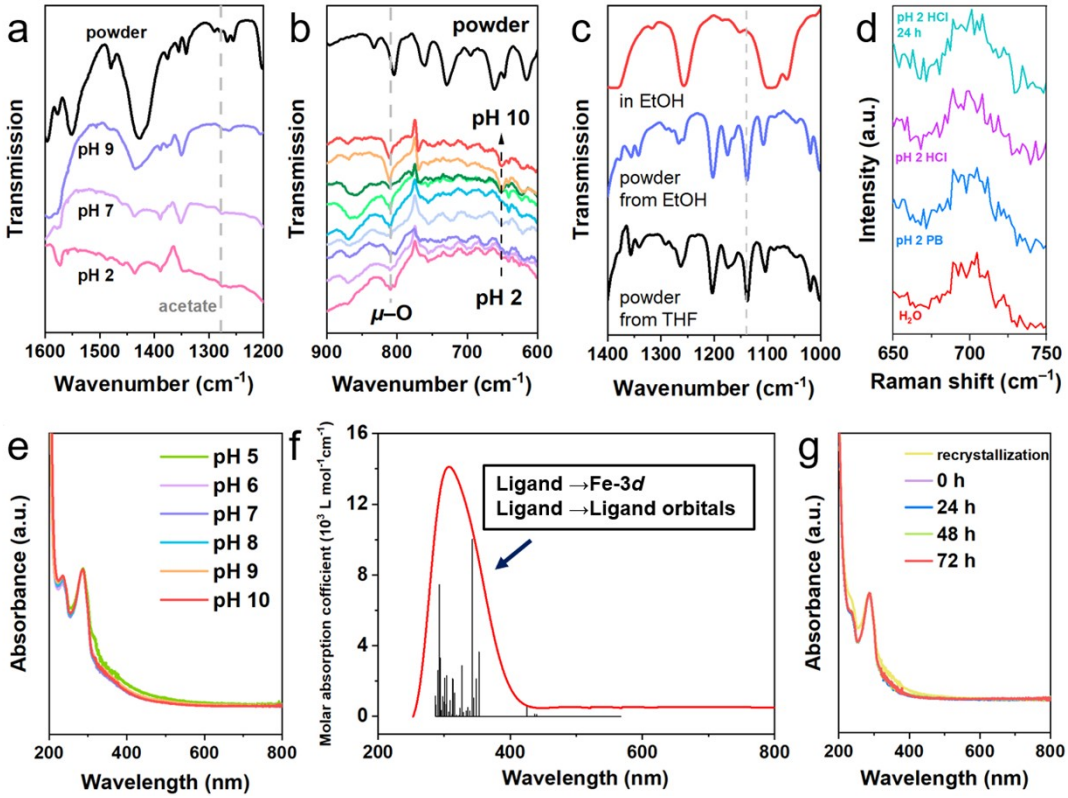

Fig. S10. Stability of complex **I** in water oxidation. **a–c)** FT-IR spectra and **d)** Raman spectra of complex **I** under different conditions; **e)** pH-dependent UV-Vis spectra of complex **I** (~ 5 mM) in phosphate buffer; **f)** The TD-DFT-calculated electronic absorption spectrum of complex **I**; **g)** Time dependent UV-Vis spectra of complex **I** (~ 5 mM) in pH 7 phosphate buffer.

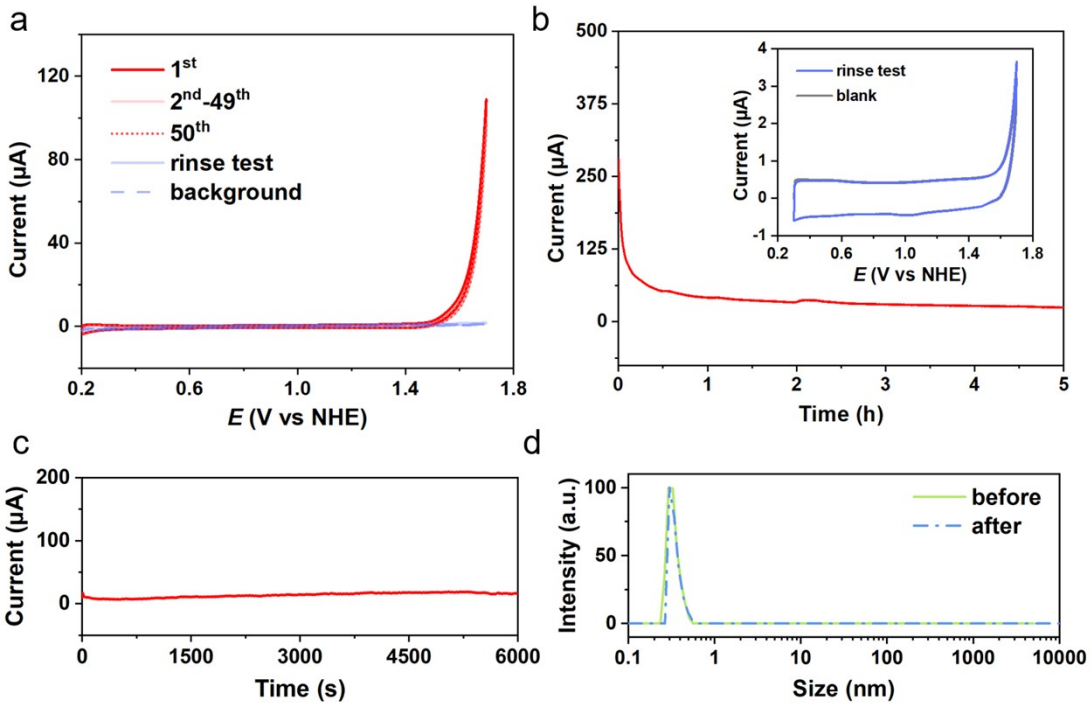

Fig. S11. a) CVs of complex **I** (0.20 mM) in a phosphate buffer solution (pH 7, 50 cycles, 1 cm^2 FTO electrode, 50 mV s^{-1}). Blue solid line: the electrode after 50 scans followed by rinsing and replacement in a fresh background solution, blue dashed line: fresh electrode in blank pH 7 phosphate buffer solution; **b)** Time dependence of electrode current by using FTO (with an exposed area of 1 cm^2) as working electrode in pH 2 phosphate buffer; **c)** Current/coulometry vs time data obtained during the CPE of complex **I** at 1.4 V vs NHE (in MeCN with 0.1 M Et_4NClO_4); **d)** Particle size distribution in phosphate buffer containing complex **I** determined by DLS measurements before and after CPE.

Tab. S4. The contents of Fe in electrolyte measured by ICP-OES.

Theoretical value		Experiment (ICP-OES)	
[complex **I**]	[Fe]	[Fe] before CPE	[Fe] after CPE
0.20 mM	1.20 mM	1.25 mM	1.21 mM

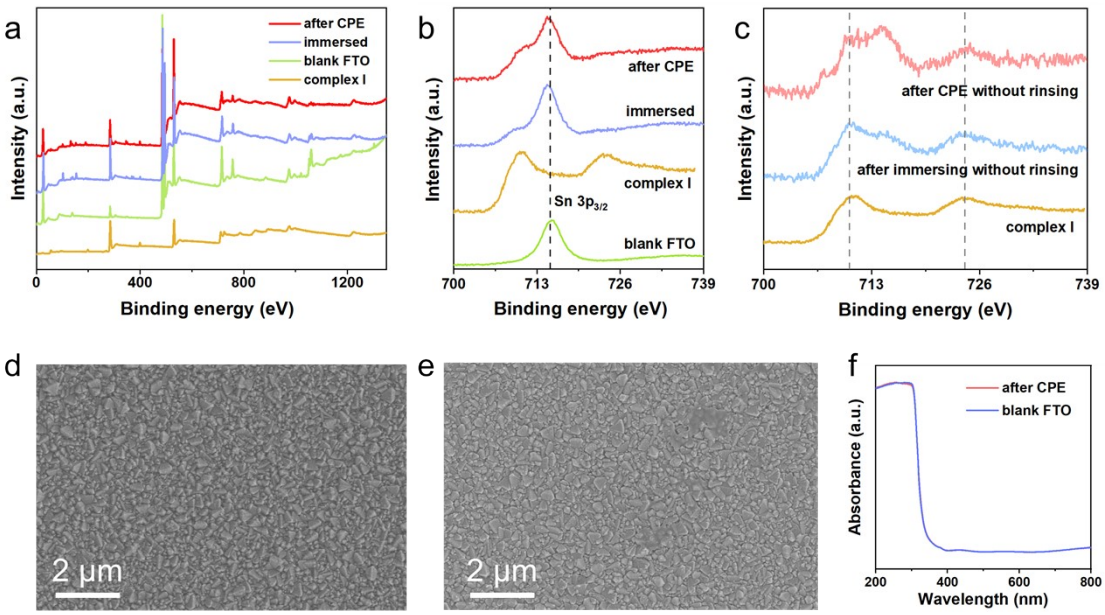

Fig. S12. a) survey XPS and **b–c)** high-resolution Fe 2p spectra of complex **I**, fresh FTO electrode, FTO electrode immersed in electrolyte for 2 h and FTO electrode after electrolysis under 1.70 V vs NHE for 2 h; SEM images of **d)** fresh FTO electrode and **e)** after electrolysis under 1.70 V vs NHE for 2 h; **f)** UV-Vis spectra of fresh FTO electrode and after electrolysis under 1.70 V vs NHE for 2 h. The FTO electrodes were rinsed with deionized water before XPS, SEM, and UV-vis analysis.

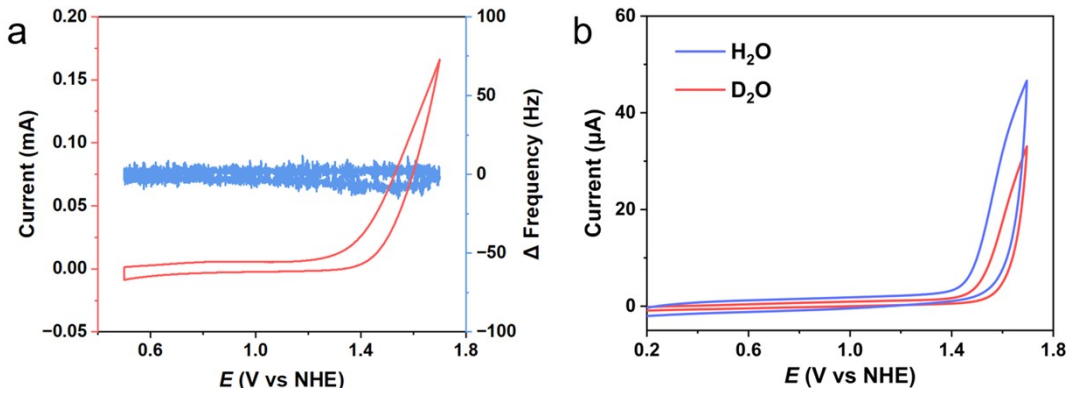

Fig. S13. a) Results of EQCM experiment of 0.25 mM complex **I** in pH 7 phosphate buffer with a gold working electrode. **b)** Kinetic isotope effect experiment (0.20 mM complex **I**, in a phosphoric acid buffer solution, pH 7, at 50 mV s^{-1}).

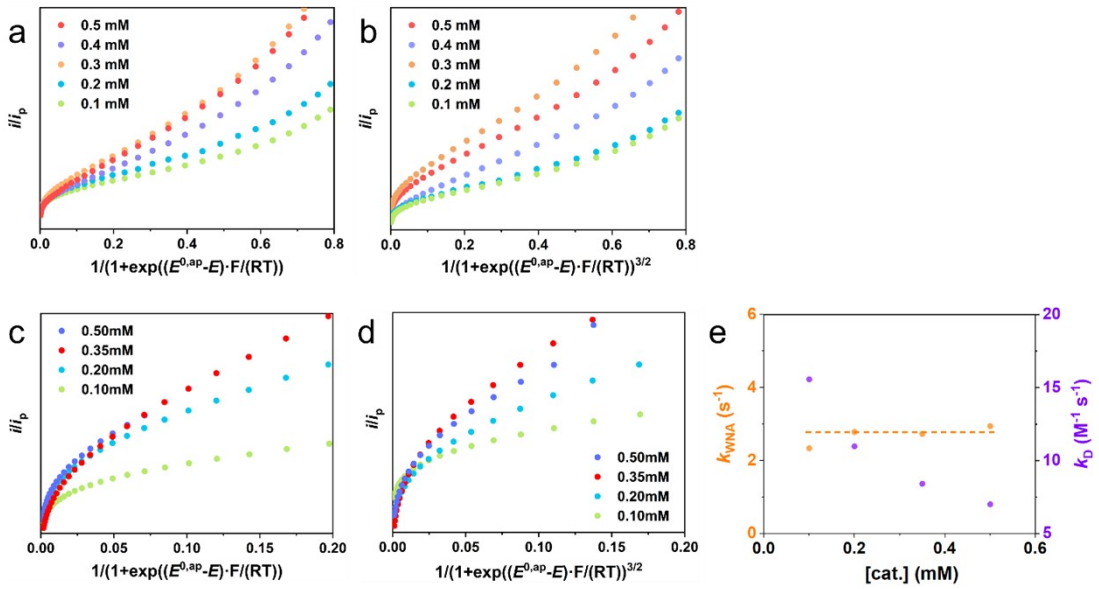

Fig. S14. FOWA measurements of complex **I**. i/i_p vs 1/{1+exp[(E_0-E)F/(RT)]} plots under different catalyst concentration assuming a WNA mechanism under **a)** pH 4 and **c)** pH 7; i/i_p vs $1/\{1+\exp[(E_0\text{-}E)F/(RT)]\}^{3/2}$ plots under different catalyst concentration assuming a I2M mechanism under **b)** pH 4 and **d)** pH 7. The original CVs are shown in Fig. S4d and Fig. S4e; **e)** Plot of calculated k_D and k_{WNA} vs. [cat.] for FOWA in pH 7.

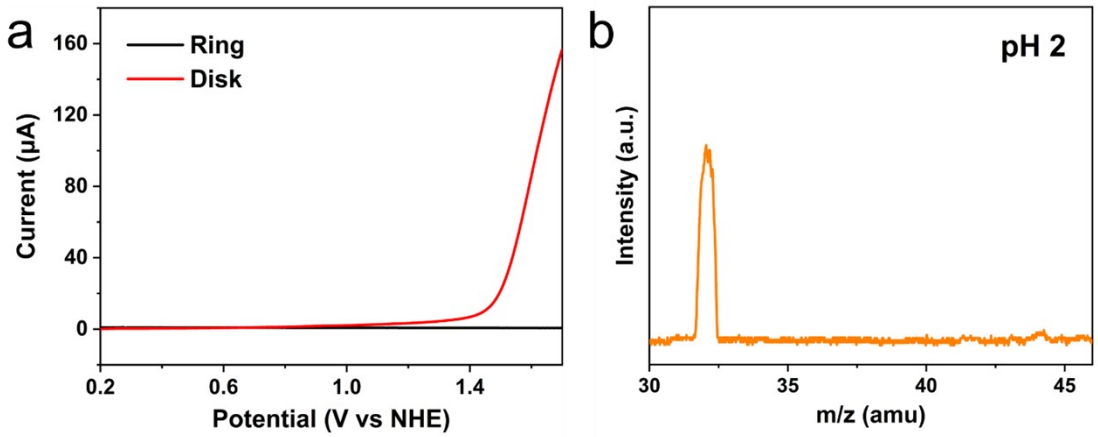

Fig. S15. a) Rotating ring (Pt) disk (GC) electrode analysis 0.5 mM complex **I** in a pH 7 phosphoric acid buffer solution, with a ring electrode potential of 0.94 V vs NHE. The rotation rate is 1600 rpm, and the scan rate is 50 mV s^{-1}; **b)** DEMS signals during water oxidation (1.70 V vs NHE) by complex **I** (0.25 mM) in phosphate buffer (pH 2) contain $H_2{}^{16}O$.

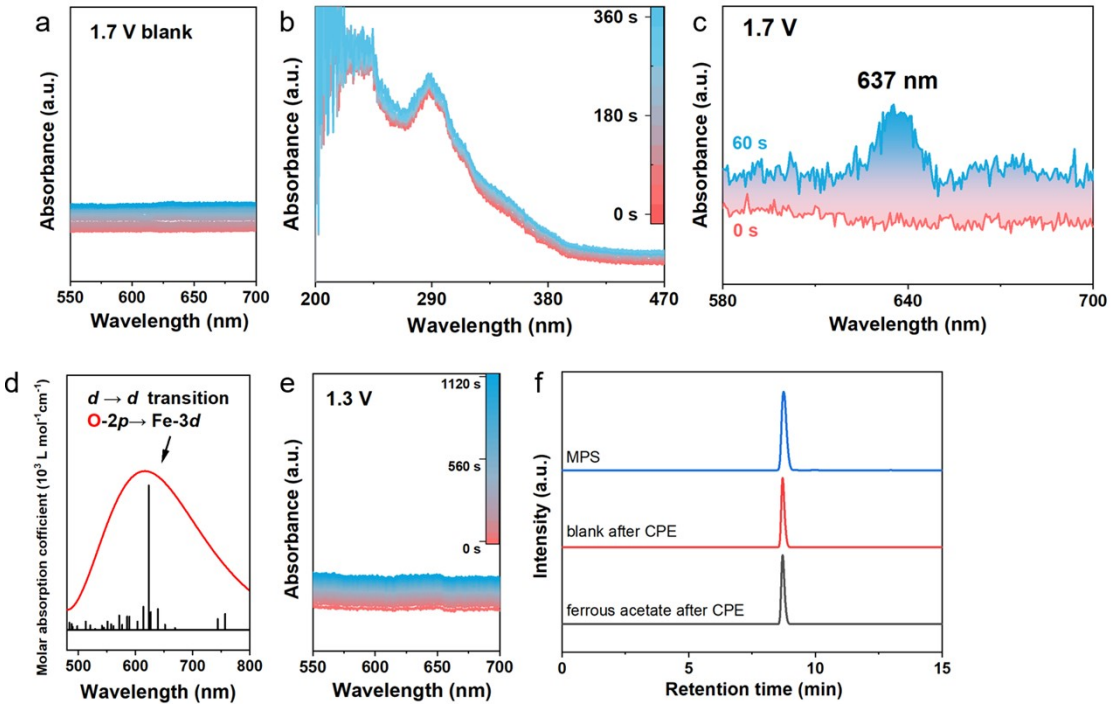

Fig. S16. In situ spectra of complex **I**. Spectroelectrochemistry monitoring change in optical absorption spectrum during water oxidation. **a)** in blank phosphate buffer under 1.70 V vs NHE; **b)** 0.25 mM complex **I** in pH 7 phosphate buffer solution under 1.70 V vs NHE. **c)** 0.25 mM complex **I** in pH 7 phosphate buffer. Blue and red: before and after applying a potential of 1.70 V vs NHE for 60 s, respectively. **d)** The TD-DFT-calculated electronic absorption spectrum. **e)** 0.25 mM complex **I** in pH 7 phosphate buffer solution under 1.30 V vs NHE. **f)** HPLC profiles of blank electrolyte (acetonitrile, with 5% H_2O, 0.1 M Et_4NClO_4 and 1 mM MPS) and in the presence of a Fe salt (ferrous acetate) after CPE (1.70 V vs NHE) for 2 h.

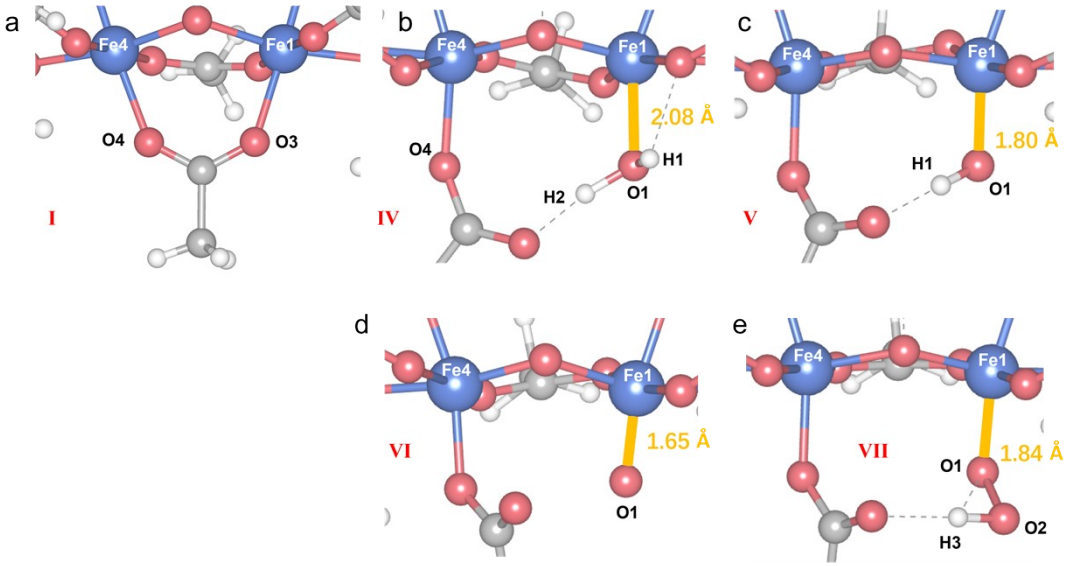

Fig. S17. Structural details of **a) I**; **b) IV**; **c) V**; **d) VI**; and **e**) **VII**.

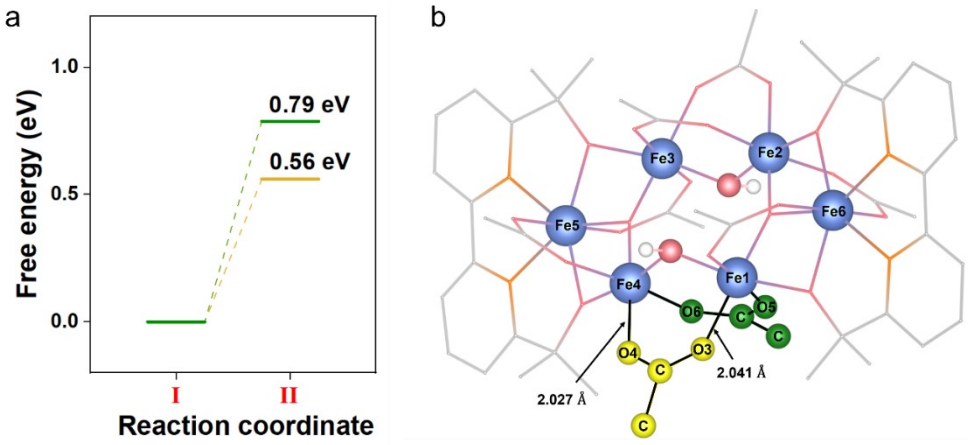

Fig. S18. a) The free energy barrier for disconnecting different acetate ligands during the water nucleophilic attach process (yellow: Fe1–O3, green: Fe1–O5); **b)** Structural model with the two acetate ligands (between Fe1 and Fe4) highlighted and the lengths of Fe1–O3, Fe4–O4 bonds noted.

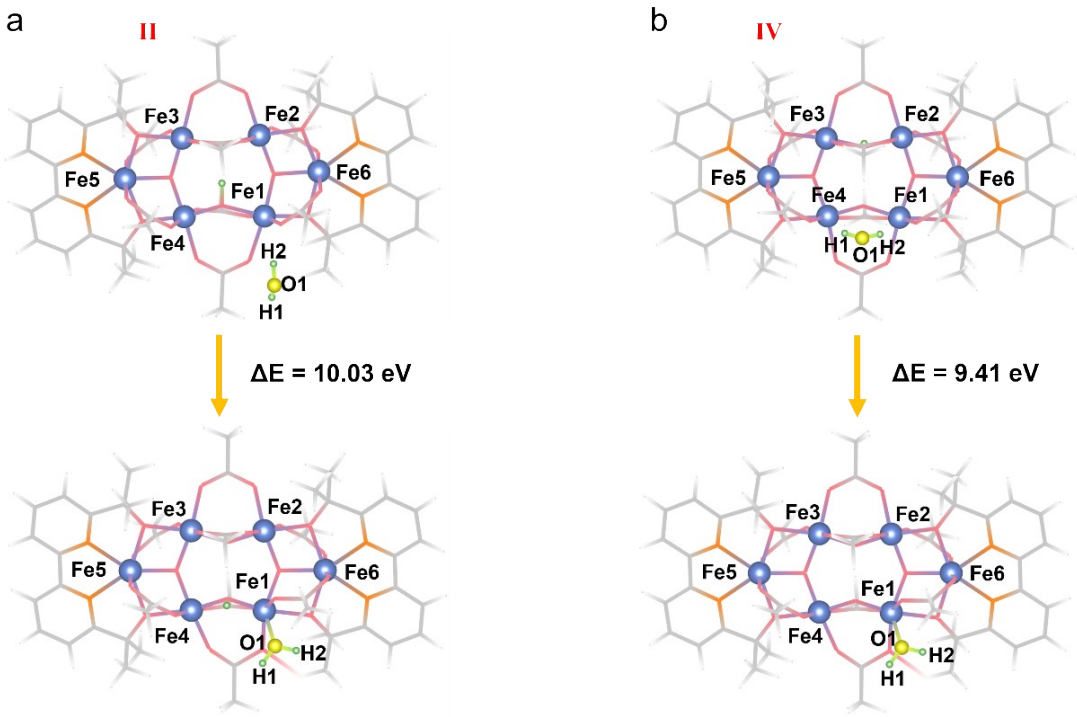

Fig. S19. The initial and optimized structures. **a)** species **II** and **b)** species **IV** without the bond breaking between Fe1 and O1 in the acetate ligand. The water molecule is unable to be attached in both cases.

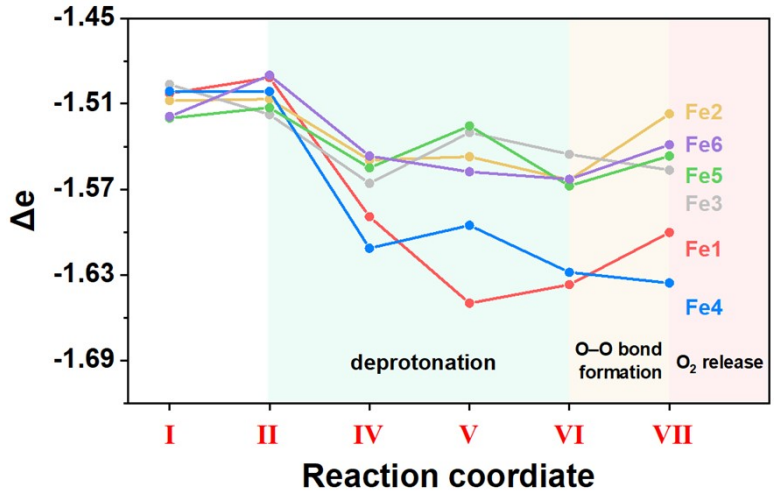

Fig. S20. The net electron change of the six iron atoms during path **1** based on Bader charge analysis.

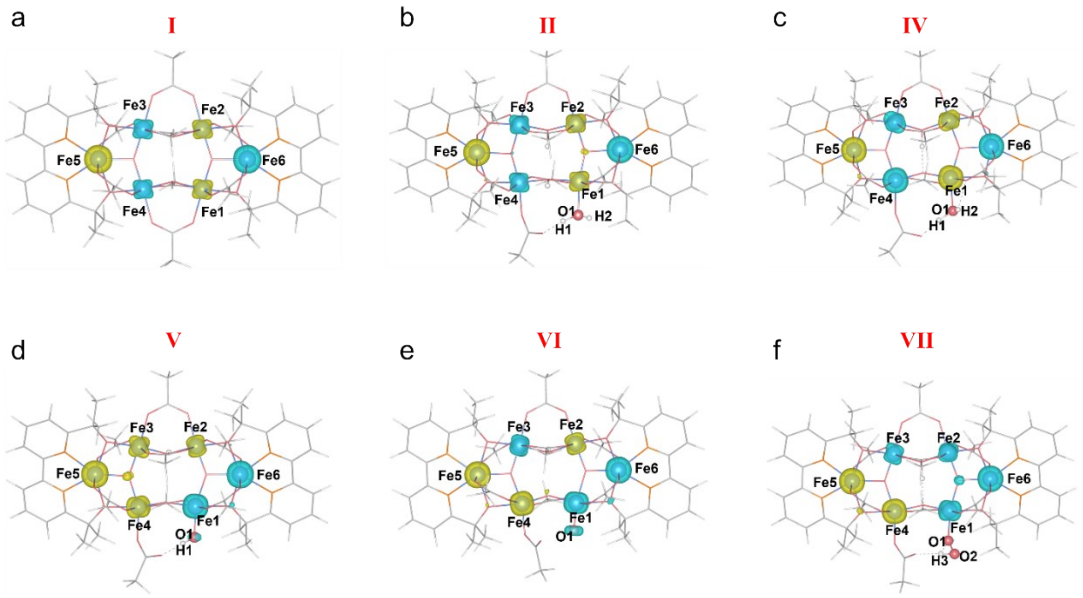

Fig. S21. Spin density distribution. **a)** complex **I**; **b) II**; **c) IV**; **d) V**; **e) VI**; and **f) VII**. The spin-up and spin-down polarizations are distinguished by yellow and blue colors. The isosurface is set to ± 0.05 e/Bohr^3.

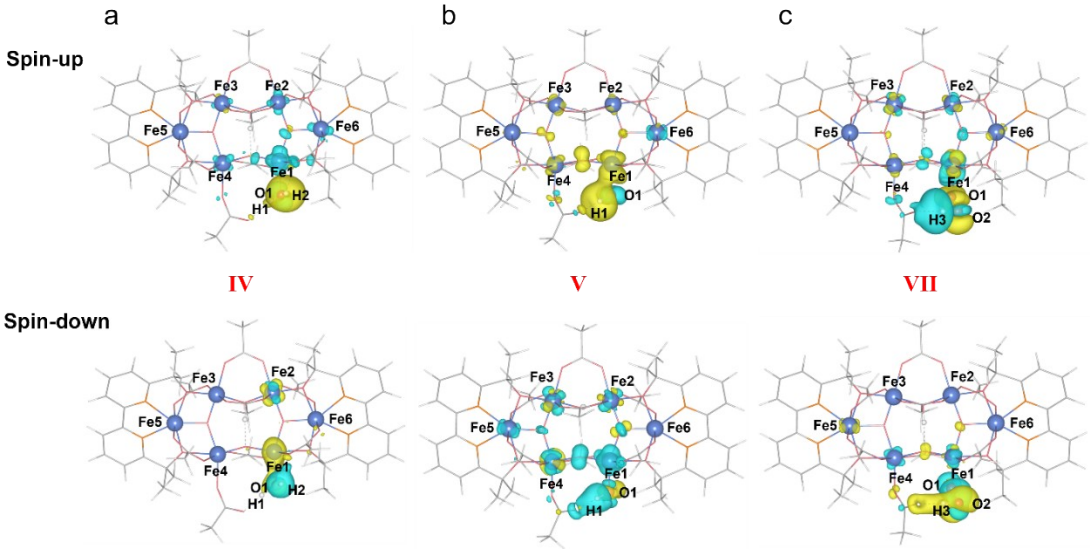

Fig. S22. Differential charge density distribution of spin-up and spin-down electrons. **a)** disconnecting H2 in **IV**; **b)** disconnecting H1 in **V**; and **c)** connecting –OH (from the second attack water molecule) in **VII**. The electron accumulation and depletion are represented by yellow and blue colors, respectively. The isosurface values are set to ± 0.003 e/Bohr^3.

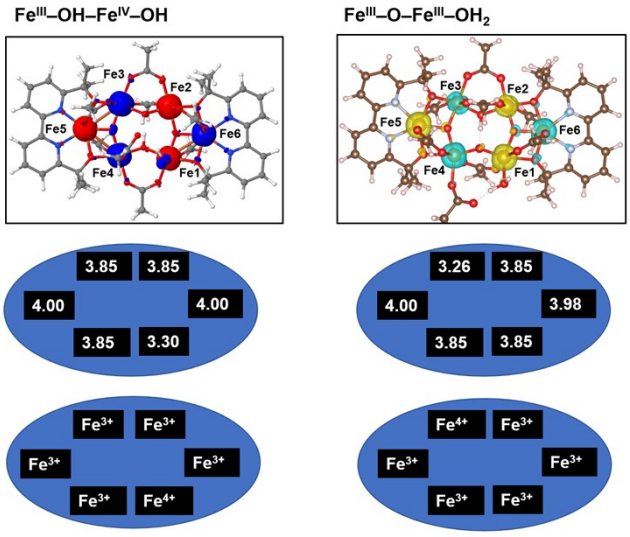

Fig. S23. Oxidation state of iron atoms in **III** to **IV** of path 1 in Fig. 4a.

FM

(a) Initial input spin orientation

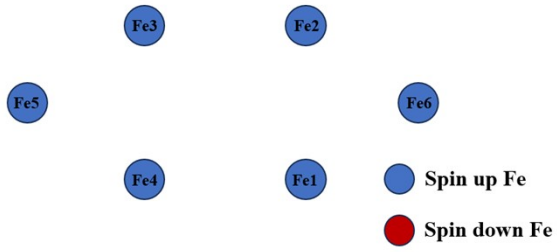

(b) Fe^{2+}-HS

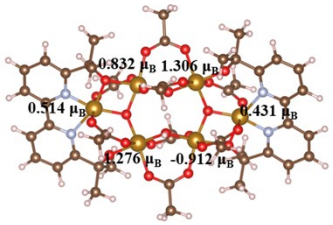

E_{tot} = -910.31269 eV

(c) Fe^{3+}-LS

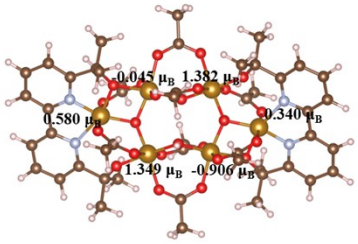

E_{tot}= -910.21781 eV

(d) Fe^{3+}-HS

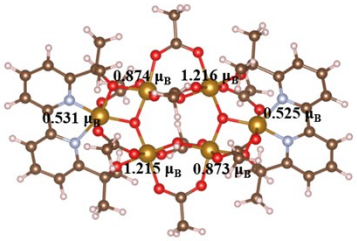

E_{tot}= -910.37686 eV

AFM-1

(a) Initial input spin orientation

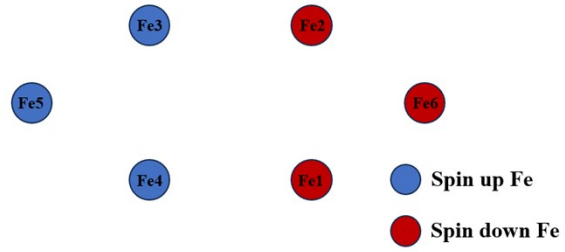

(b) Fe^{2+}-HS

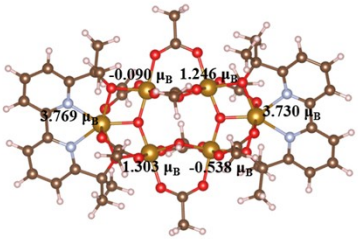

E_{tot} = -911.19785 eV

(c) Fe^{3+}-LS

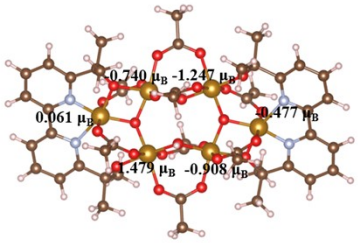

E_{tot}= -910.33337eV

(d) Fe^{3+}-HS

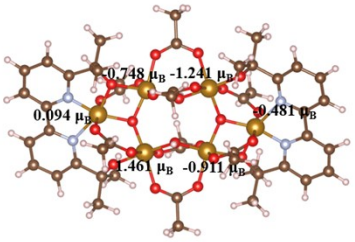

E_{tot}= -910.31318 eV

AFM-2

(a)

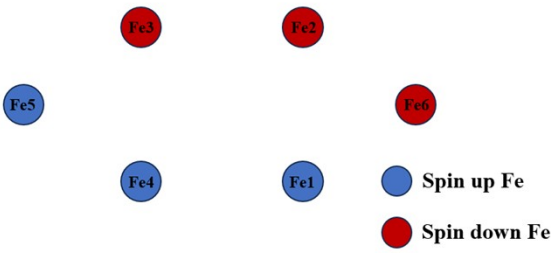

(b)

Fe^{2+}-HS

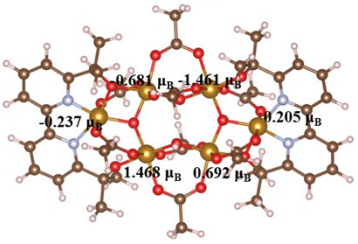

E_{tot} = -910.27382 eV

(c)

Fe^{3+}-LS

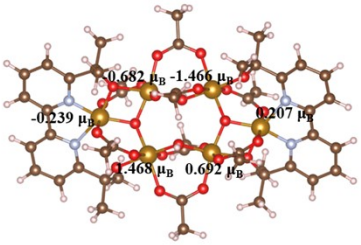

E_{tot}= -910.27116 eV

(d)

Fe^{3+}-HS

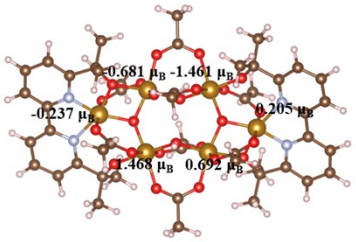

E_{tot}= -910.25245 eV

AFM-3

(a)

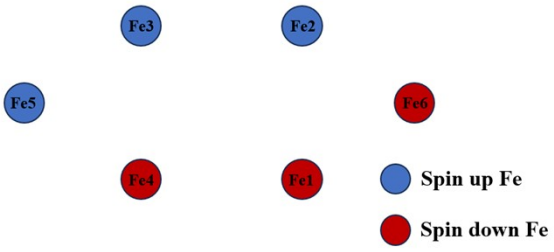

(b)

Fe^{2+}-HS

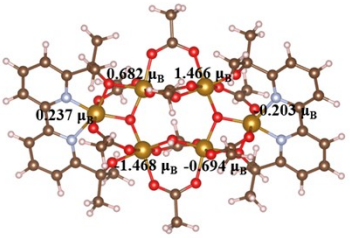

E_{tot} = -910.27151 eV

(c)

Fe^{3+}-LS

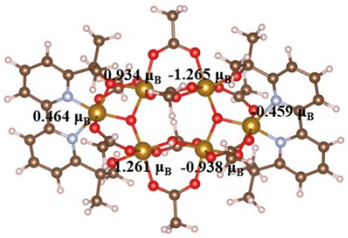

E_{tot}= -910.36442eV

(d)

Fe^{3+}-HS

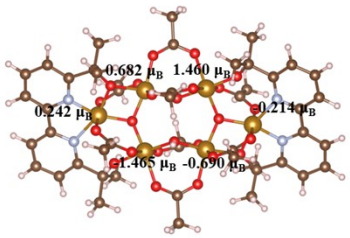

E_{tot}= -910.25074 eV

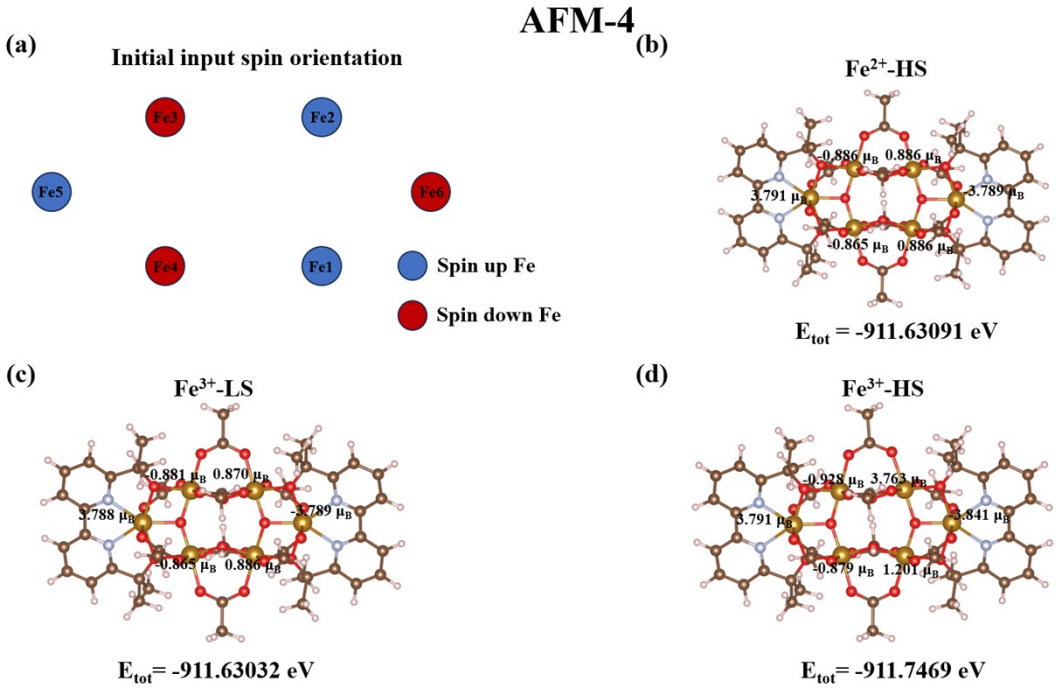

Fig. S24. The output spin polarization and the counterpart of the structures.

Tab. S5. The spin polarization of different Fe and total energy for complex **I** during the optimization process.

Input Spin Polarization (μ_B)									Output Spin Polarization (μ_B)						Total Energy (eV)
Magnetic Order	Oxidation States	Spin States	Fe1	Fe2	Fe3	Fe4	Fe5	Fe6	Fe1	Fe2	Fe3	Fe4	Fe5	Fe6	
FM	Fe^{2+}	HS	4.000	4.000	4.000	4.000	4.000	4.000	-0.912	1.306	0.832	1.276	0.514	0.431	-910.313
	Fe^{3+}	LS	1.000	1.000	1.000	1.000	1.000	1.000	-0.906	1.382	-0.045	1.349	0.580	0.380	-910.218
		HS	5.000	5.000	5.000	5.000	5.000	5.000	0.873	1.216	0.874	1.215	0.531	0.525	-910.377
AFM-1	Fe^{2+}	HS	-4.000	-4.000	4.000	4.000	4.000	-4.000	-0.538	1.246	-0.090	1.303	3.796	-3.730	-911.198
	Fe^{3+}	LS	-1.000	-1.000	1.000	1.000	1.000	-1.000	-0.908	-1.247	-0.740	1.479	0.061	-0.477	-910.333
		HS	-5.000	-5.000	5.000	5.000	5.000	-5.000							
AFM-2	Fe^{2+}	HS	4.000	-4.000	-4.000	4.000	4.000	-4.000	0.692	-1.461	-0.681	1.468	-0.237	0.205	-910.274
	Fe^{3+}	LS	1.000	-1.000	-1.000	1.000	1.000	-1.000							
		HS	5.000	-5.000	-5.000	5.000	5.000	-5.000							
AFM-3	Fe^{2+}	HS	-4.000	4.000	4.000	-4.000	4.000	-4.000	-0.694	1.466	0.682	-1.468	0.237	-0.203	-910.272
	Fe^{3+}	HS	-5.000	5.000	5.000	-5.000	5.000	-5.000							
		LS	-1.000	1.000	1.000	-1.000	1.000	-1.000	-0.938	-1.265	0.934	1.261	0.464	-0.459	-910.364
AFM-4	Fe^{2+}	HS	4.000	4.000	-4.000	-4.000	4.000	-4.000	0.886	0.886	-0.886	-0.865	3.791	-3.789	-911.631
	Fe^{3+}	LS	1.000	1.000	-1.000	-1.000	1.000	-1.000							
		HS	5.000	5.000	-5.000	-5.000	5.000	-5.000	1.201	3.763	-0.928	-0.879	3.791	-3.841	-911.75

Tab. S6. Comparison of bond lengths and angles from X-ray crystal structure and optimized structure by VASP.

	Experiment	Calculation
Fe1–(μ_2-O)	1.968 Å	1.886 Å
Fe4–(μ_2-O)	1.954 Å	1.886 Å
Fe3–(μ_3-O)	1.882 Å	1.771 Å
Fe4–(μ_3-O)	1.854 Å	1.771 Å
Fe5–(μ_3-O)	1.935 Å	1.984 Å
Fe1–(μ_2-O)–Fe4	124.2°	124.8°

References

1 B. Rudshteyn, K. J. Fisher, H. M. C. Lant, K. R. Yang, B. Q. Mercado, G. W. Brudvig, R. H. Crabtree and V. S. Batista, *ACS Catal.*, 2018, **8**, 7952–7960.

2 G. M. Sheldrick, *Acta Crystallogr A Found Crystallogr*, 2008, **64**, 112–122.

3 W. Guo, Z. Shen, Y. Su, K. Li, W. Lin, G. Chen, J. Guan, X. Wang, Z. Li, Z. Yu and Z. Zou, *Dalton Trans.*, 2022, **51**, 12494–12501.

4 J. Xie, P. Yang, C. Tang, T. Chen, C. Zhong, L. Wang and Y. Huang, *Adv. Mater. Interfaces*, 2021, **8**, 2101069.

5 M. Okamura, M. Kondo, R. Kuga, Y. Kurashige, T. Yanai, S. Hayami, V. K. K. Praneeth, M. Yoshida, K. Yoneda, S. Kawata and S. Masaoka, *Nature*, 2016, **530**, 465–468.

6 K. G. Kottrup, S. D'Agostini, P. H. van Langevelde, M. A. Siegler and D. G. H. Hetterscheid, *ACS Catal.*, 2018, **8**, 1052–1061.

7 R. Matheu, S. Neudeck, F. Meyer, X. Sala and A. Llobet, *ChemSusChem*, 2016, **9**, 3361–3369.

8 Q. Huang, S. Xie, J. Hao, Z. Ding, C. Zhang, H. Sheng and J. Zhao, *Angew. Chem. Int. Ed.*, 2023, **62**, e202300469.

9 L. L. Williams and R. D. Webster, *J. Am. Chem. Soc.*, 2004, **126**, 12441–12450.

10 G. Kresse and J. Furthmüller, *Phys. Rev. B*, 1996, **54**, 11169–11186.

11 P. E. Blöchl, *Phys. Rev. B*, 1994, **50**, 17953–17979.

12 J. P. Perdew, K. Burke and M. Ernzerhof, *Phys. Rev. Lett.*, 1996, **77**, 3865–3868.

13 H. J. Monkhorst and J. D. Pack, *Phys. Rev. B*, 1976, **13**, 5188–5192.

14 M. R. Hestenes and E. Stiefel, *Journal of research of the National Bureau of Standards*, 1952, **49**, 409–436.

15 V. I. Anisimov, J. Zaanen and O. K. Andersen, *Phys. Rev. B*, 1991, **44**, 943–954.

16 F. Neese, *WIREs Comput Mol Sci*, 2012, **2**, 73–78.

17 J. P. Perdew, *Phys. Rev. B*, 1986, **33**, 8822–8824.

18 S. Grimme, S. Ehrlich and L. Goerigk, *J. Comput. Chem.*, 2011, **32**, 1456–1465.

19 F. Weigend and R. Ahlrichs, *Phys. Chem. Chem. Phys.*, 2005, **7**, 3297.

20 R. Bauernschmitt, M. Häser, O. Treutler and R. Ahlrichs, *Chem. Phys. Lett.*, 1997, **264**, 573–578.

21 E. Runge and E. K. U. Gross, *Phys. Rev. Lett.*, 1984, **52**, 997–1000.

22 R. E. Stratmann, G. E. Scuseria and M. J. Frisch, *J. Chem. Phys.*, 1998, **109**, 8218–8224.

23 T. Lu and F. Chen, *J. Comput. Chem.*, 2012, **33**, 580–592.

24 Y. Wang, X. Lei, B. Zhang, B. Bai, P. Das, T. Azam, J. Xiao and Z. Wu, *Angew. Chem. Int. Ed.*, 2023, e202316903.

25 R. Chalil Oglou, T. G. Ulusoy Ghobadi, F. S. Hegner, J. R. Galán-Mascarós, N. López, E. Ozbay and F. Karadas, *Angew. Chem. Int. Ed.*, 2023, **62**, e202308647.

26 C. Bozal-Ginesta, R. R. Rao, C. A. Mesa, Y. Wang, Y. Zhao, G. Hu, D. Antón-García, I. E. L. Stephens, E. Reisner, G. W. Brudvig, D. Wang and J. R. Durrant, *J. Am. Chem. Soc.*, 2022, **144**, 8454–8459.

27 A. Dey, A. Guha, V. Kumar, S. Bawari, T. N. Narayanan and V. Chandrasekhar, *Dalton Trans.*, 2021, **50**, 14257–14263.

28 M. Licini and J. A. Gareth Williams, *Chem. Commun.*, 1999, **19**, 1943–1944.

29 V. K. K. Praneeth, M. Kondo, M. Okamura, T. Akai, H. Izu and S. Masaoka, *Chem. Sci.*, 2019, **10**, 4628–4639.
30 M. N. Akhtar, R. Bikas, M. A. AlDamen, Z. Shaghaghi, M. Shahid and A. Sokolov, *Dalton Trans.*, 2022, **51**, 12686–12697.
31 H. Zhang, X. Su, F. Xie, R. Liao and M. Zhang, *Angew. Chem. Int. Ed.*, 2021, **60**, 12467–12474.
32 S. Mehrabani, R. Bikas, Z. Zand, Y. Mousazade, S. I. Allakhverdiev and M. M. Najafpour, *Int. J. Hydrog. Energy*, 2020, **45**, 17434–17443.